

A one-dimensional continuous model for carbon nanotubes

Xiaohua Zhou*

Department of Mathematics and Physics, Fourth Military Medical University, Xi'an 710032, China

(Dated: March 6, 2018)

The two-dimensional (2D) continuous elastic energy model for isotropic tubes is reduced to a one-dimensional (1D) curvature elastic energy model strictly. This 1D model is in accordance with the Kirchhoff elastic rod theory. Neglecting the in-plane strain energy in this model, it is suitable to investigate the nature features of carbon nanotubes (CNTs) with large deformations and can also reduce to the string model in [Z.C. Ou-Yang *et al.*, Phys. Rev. Lett. **76** 4055 (1997)] when the deformation is small enough. For straight chiral shapes, this general model indicates that the difference of the chiral angle between two equilibrium states is about $\pi/6$, which is consistent with the lattice model. It also reveals that the helical shape has lower energy for per atom than the straight shape has in the same condition. By solving the corresponding equilibrium shape equations, the helical tube solution is in good agreement with the experimental result, and super helical shapes are obtained and we hope they can be found in future experiments.

I. INTRODUCTION

In the past two decades, the CNTs initially synthesized by Iijima [1] attracted many researchers' attention due to the excellent physical characteristics and potential applications in many apparatus and nano-instruments, such as field emission sources [2], probe tips [3, 4] and quantum wires [5]. Experiments indicate that the configurations of CNTs, such as their radii, lengths and helicity, strictly determine their physical capability, but it is difficult to precisely control those configurations during production processes. So, although the CNT is a particularly important functional nanomaterial, obtaining macroscopical bulk materials is a challenging problem [6]. Recently, an important progress reported by Davis *et al.* [7] shows a way to obtain macroscopical fibres of the SWNTs using the self-assemble method in chlorosulphonic acid. Moreover, the mechanical parameters of CNTs are not unification due to the size effect, which confines their applications as a reliable high strength material. For instance, the Young's modulus will decline with the increase of the diameters of CNTs [8]. The above problems indicate that there are still some challenges to overcome before we can widely put CNTs in practice.

An interesting phenomenon is that CNTs often present as beelines (including zigzag and armchair shapes [9–11]), helixes [12, 14, 15] as well as rings [16, 17]. And a possible reason for those shapes is the thermodynamic effects in different synthesizing methods. Particularly, periodic defects (heptagon and pentagon cells) play an important rule in the forming of helical shapes [12, 18]. SWNTs are generally taken as a frizzy graphite layer and multi-walled carbon nanotubes (MWNTs) consist of multiple rolled layers of graphite. Many physical properties of the CNT are obtained by calculating the interaction between its carbon lattices. There are also many researchers who take the CNT as 2D continuous tubules [19–22]. Ou-Yang *et al.* [19] continued the lattice model which provided by Lenosky *et al.* [23] and pointed out that SWNT's free energy is similar to the model for vesicles [24] when ignored the in-plane strain energy. In Refs. [21, 22] Tu and Ou-Yang provided a general 2D model which considered the in-plane strain energy and revealed that the effective Young's modulus of MWNTs depends on the layer number.

Although the CNT is taken as the 1D elastic material, by far there is still not a strict model to connect the lattices model and the Kirchhoff elastic rod theory. The string model [19] provided a recommendable way to make up this missing link, but it cannot be used to investigate the mechanical behaviors when outside forces act on CNTs, because the in-plane strain energy can not be ignored in this circumstance. So it needs to construct a complete 1D model which should contain the in-plane strain energy to connect the lattices model and the Kirchhoff theory. Besides, although the lattice model can geometrically tell us that the defects induce the helical shapes, it lacks a reasoned physical theory to expound the reason of the emergence of helical CNTs. Can the continuous model explain why there are so many helical CNTs? Further, considering that 1D structures can form super helical shapes, such as DNA chains, so can we obtain super helical CNTs? These questions need to be investigated deeply. Not only will they help us to understand the physical characters of the low dimensional systems, they will provide us with new materials and methods to design nano-instruments. In this paper, we will give a complete 1D continuous CNTs model which contains the in-plane strain energy to discuss the above problems. This paper is organized as follows: In Sec. II, the

*Electronic address: xhzhou08@gmail.com

2D continuous elastic shell model is reduced to a 1D curvature elastic model strictly. This complete 1D model is in accordance with the isotropic Kirchhoff elastic rod model and is suitable to investigate the mechanical behaviors of CNTs. In Sec. III, a concise model which ignores the in-plane strain energy is used to study the nature features of CNTs. By solving the corresponding shape equations, the helical solution is in good agreement with the experimental result and super helical shapes are obtained. Finally, a short discussion is presented in Sec. IV.

II. A COMPLETE 1D MODEL FOR ISOTROPIC ELASTIC TUBES AND CNTS

Let the central line of an elastica tube be $\mathbf{R} = \mathbf{R}(s)$, $\vec{\alpha} = \dot{\mathbf{R}}$ be the tangent vector (an overdot denotes differential with respect to s which is the arclength of the central line of the tube), $\vec{\beta} = \ddot{\mathbf{R}}/K$ be the main normal vector and $\vec{\gamma} = \vec{\alpha} \times \vec{\beta}$ be the binormal vector, between those unit vectors, there are the Frenet formulae: $d\vec{\alpha}/ds = K\vec{\beta}$, $d\vec{\beta}/ds = -K\vec{\alpha} + \tau\vec{\gamma}$ and $d\vec{\gamma}/ds = -\tau\vec{\beta}$, where K and τ are the curvature and torsion [25] of the central line \mathbf{R} , respectively. The shape of the tube can be obtained by this way: the central point of a ring with the radius r_0 moves along a line \mathbf{R} and keeps the ring upright to the tangent of \mathbf{R} . It means the ring is in the normal plane of the central line \mathbf{R} . Let \mathbf{Y} be the shape of the tube, there is

$$\mathbf{Y} = \mathbf{R} + \mathbf{r} = \mathbf{R} + r_0 \cos \theta \vec{\beta} + r_0 \sin \theta \vec{\gamma}, \quad (1)$$

where the parameter $0 \leq \theta \leq \pi/2$. Using the Frenet formulae, we obtain the mean curvature and Gaussian curvature: $H = \frac{1-2r_0K \cos \theta}{2r_0(r_0K \cos \theta - 1)}$ and $\Lambda = \frac{K \cos \theta}{r_0(r_0K \cos \theta - 1)}$, respectively. Here we give a method in appendix A to show how to attain these two curvatures. The 2D curvature elastic energy of a tube is [21, 26–29]

$$F_s = \frac{Yh^3}{24(1-\nu^2)} \oint [(2H)^2 - 2(1-\nu)\Lambda] d\sigma, \quad (2)$$

where Y is the Young's modulus, ν is the Poisson ratio, h is the thickness of the tube and $d\sigma$ is the area element. The above energy derives from bending the graphene to SWNTs. For any compact, closed 2D surface, $\oint \Lambda d\sigma$ is a constant because there is the Gauss-Bonnet theorem [31]

$$\oint \Lambda d\sigma = 2\pi E_r, \quad (3)$$

where E_r is the Euler characteristic which only depends on the topological structure of the surface. For spherical topology surface, there is $E_r = 2$. For torus, cylinders and tubes with infinite length, there is $E_r = 0$. In the following text, we will study the torus and tubes with infinite length, so we eliminate the constant term associated with $\oint \Lambda d\sigma$ in (2). Considering $d\sigma = r_0(1 - r_0K \cos \theta)d\theta$ and $r_0^2K^2 < 1$, and using the Euler integral, Eq. (2) is reduced to

$$F_s = \frac{\pi Y h^3}{12 r_0 (1 - \nu^2)} \int \frac{1}{\sqrt{1 - r_0^2 K^2}} ds. \quad (4)$$

The in-plane strain energy can be expressed as [26–29]

$$F_i = \frac{Yh}{2(1-\nu^2)} \oint [(\varepsilon_x + \varepsilon_y)^2 - 2(1-\nu)(\varepsilon_x \varepsilon_y - \varepsilon_{xy}^2)] d\sigma, \quad (5)$$

where ε_x , ε_y and ε_{xy} are the axial, circumferential, and shear strains, respectively. In Fig. 1(a), we show a fragment of SWNT with the radius r_0 and the length of its central line is ds . We suppose that its central line has a bend angle $d\phi$, so the radius of curvature is $R = 1/K = ds/d\phi$. Taking the SWNT as an isotropic elastic tube and the central line is nonretractable, and supposing that the initial state is a straight tube, from Fig. 1 we can see that the protraction of the point P along the axis direction is $ds_0 = [R - r_0 \cos(\theta + d\theta)]d\phi - ds \simeq -r_0 \cos \theta d\phi$. Then the tensile strain on point P is $\varepsilon_x = \frac{ds_0}{ds} = -r_0 K \cos \theta$. We simply choose the circumferential strain $\varepsilon_y = -\nu \varepsilon_x = \nu r_0 K \cos \theta$. Correspondingly, the shear strain on point P is $\varepsilon_{xy} = \frac{1}{2} r_0 \frac{d\theta}{ds}$. Note $\frac{d\theta}{ds} = \tau + \frac{d\chi}{ds}$, there is $\varepsilon_{xy} = r_0(\tau + \dot{\chi})/2$. Here the definitions of θ and χ please see the caption of Fig. 1. Using the above results, Eq. (5) is reduced to

$$F_i = \frac{\pi r_0^3 Y h}{2(1+\nu)} \int [(1+\nu)K^2 + (\tau + \dot{\chi})^2] ds. \quad (6)$$

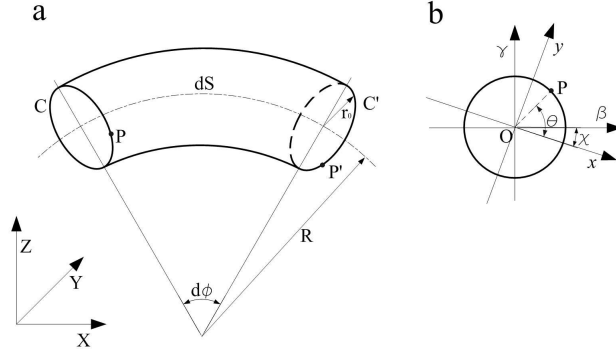


FIG. 1: (a) A fragment of a curving SWNT with the radius r_0 , the length of central line ds and the bending angle $d\phi$, C and C' are the cross section rings on the two ends. (b) The left cross section of the SWNT. $\vec{\beta}$ and $\vec{\gamma}$ are the main normal vector and the binormal vector of the central line, respectively. (x, y, z) are the local coordinates with the x, y axes fixed on the cross section ring and with the z axis superposed to the tangent of the central line. χ is the angle between $\vec{\beta}$ and the x axis. Point P is fixed on the cross section ring (on the left end) and the angle between \overline{OP} and $\vec{\beta}$ is θ . When the cross section ring moves along the central line from the left end to the right end, P changes to P' (Note that the cross section ring can turn around the central axis.). In this process, the angular displacement of point P in the local coordinates (x, y, z) is $d\theta$ and the change of χ is $d\chi$. Supposing that the initial state is a straight tube, this two charts indicate the protraction of the point P along the central line is $ds_0 = -r_0 \cos \theta d\phi$, the corresponding tensile strain is $\varepsilon_x = \frac{ds_0}{ds} = -r_0 K \cos \theta$ and the shear strain is $\varepsilon_{xy} = r_0(\tau + \dot{\chi})/2$.

Then, the 1D energy density of a tube can be written as

$$\mathcal{F} = \frac{\pi Y h^3}{12 r_0 (1 - \nu^2)} \frac{1}{\sqrt{1 - r_0^2 K^2}} + \frac{\pi r_0^3 Y h}{2} K^2 + \frac{\pi r_0^3 Y h}{2(1 + \nu)} (\tau + \dot{\chi})^2. \quad (7)$$

For a multilayered tube, the energy density is

$$\mathcal{F}_m \simeq \int_{\rho_i}^{\rho_o} (\mathcal{F}/b + 2\pi r_0 g/b) dr_0, \quad (8)$$

where b is the distance of two neighbor layers, g is the surface energy density between two neighbor layers, ρ_i and ρ_o are the inmost and outmost radii, respectively. Specially, when $b = h$, there is

$$\mathcal{F}_m = \frac{\pi Y b^2}{12(1 - \nu^2)} \ln \left[\frac{\rho_o (1 + \sqrt{1 - K^2 \rho_i^2})}{\rho_i (1 + \sqrt{1 - K^2 \rho_o^2})} \right] + \frac{1}{2} Y I_r K^2 + \frac{1}{2} G I_t (\tau + \dot{\chi})^2 + P S_0, \quad (9)$$

where $I_r = \pi(\rho_o^4 - \rho_i^4)/4$ and $I_t = \pi(\rho_o^4 - \rho_i^4)/2$ are the moments of inertia of the cross section around its diameter and central axis, respectively. $G = Y/(2 + 2\nu)$ is the shear modulus, $P = g/b$ can be taken as the volumetric energy density and $S_0 = \pi(\rho_o^2 - \rho_i^2)$ is the area of the cross section of the tube. When $\rho_i = 0$, the second and the third terms in the right hand side of the above equation compose the typical isotropic Kirchhoff elastic rod model.

In Refs. [21, 22], Tu and Ou-Yang continued the lattice model and showed that the energy density for SWNTs is similar to the elastic shell model. Using their results and considering Eq. (7), the energy density for SWNTs is

$$\mathcal{F}_{sw} = \frac{A}{\sqrt{1 - r_0^2 K^2}} + \frac{B}{2} K^2 + \frac{C}{2} (\tau + \dot{\chi})^2, \quad (10)$$

where $A = \pi k_c/r_0$, $B = (1 - \nu^2)\pi r_0^3 k_d$, $C = B/(1 + \nu)$, $k_c = 1.62$ eV and $k_d = 22.97$ eV/Å² [22]. Considering $r_0^2 K^2 \ll 1$, $r_0 = 0.5 \sim 10$ nm and $B \gg \pi k_c r_0$, the first term on the right hand side of the above equations can be ignored and similar models are discussed in Refs. [30, 32] to study the mechanical properties of nanosprings. The energy density for MWNTs is

$$\mathcal{F}_{mw} \simeq \int_{\rho_i}^{\rho_o} (\mathcal{F}_{sw}/b + 2\pi r_0 g/b) dr_0, \quad (11)$$

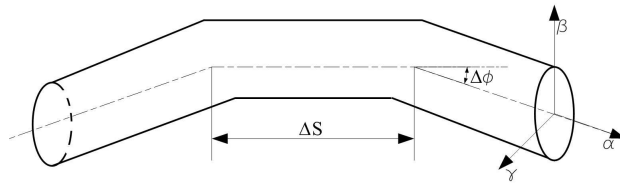


FIG. 2: A curving SWNT is composed of several straight segments connected by abrupt corners. The average length for each segment is ΔS and the average corner between two neighbor segments' central lines is $\Delta\phi$, so the curvature for the central line is $K \simeq \Delta\phi/\Delta S$.

where $b = 0.34$ nm and $g = -2.04$ eV/nm² [33]. Specially, for a straight double-walled carbon nanotube (DWNT), there is $K = \tau = 0$ in (10). Moreover, we should note that χ is just the chiral angle in this case. Considering each straight layer often has fixed chiral angle, there is $\dot{\chi} = 0$ (actually, this result means there is no strain energy, similar result will be shown in the later text), thus the energy density for a DWNT can be written as

$$\mathcal{F}_{dw} = \pi k_c \left(\frac{1}{r_0} + \frac{1}{r_0 + b} \right) + 2\pi(r_0 + b/2)g, \quad (12)$$

where r_0 is the inner radius. Choosing $k_c = 1.4$ eV [34], $\mathcal{F}_{dw} = 0$ yields

$$r_0 = 6.8 \text{ \AA}. \quad (13)$$

For dense SWNT ropes, supposing that each SWNT is continuously enveloped by its neighbors, the model in (12) can give the optimal radius for SWNTs and the similar result obtained by Zhang *et al.* is 6.8 Å [35].

In the above discussions, the energy density in (10) which contains the contribution of the in-plane deformation is suitable to study the mechanical behaviors of SWNTs. However, if we want to study the natural features of SWNTs without any outside forces, the in-plane deformation terms in (10) should be neglected. The corresponding model will be studied in the following section.

III. 1D MODEL FOR CNTS WITHOUT IN-PLANE STRAIN ENERGY

A. Analytical results

According to the experimental observation [12, 36], helical SWNTs with periodic defects can be treated as the shape in Fig. 2. Seeing Fig. 2, a SWNT is composed of several straight segments connected by abrupt corners. The average length for each segment is ΔS and the average corner between two neighbor segments' central lines is $\Delta\phi$, so the curvature for the central line is $K \simeq \Delta\phi/\Delta S$. Supposing that the average torsion angle around the $\vec{\alpha}$ axis between two neighbor segments is $\Delta\theta$ ($\Delta\theta$ here is similar to $d\theta$ in Fig. 1), there is $\tau \simeq (\Delta\theta - \Delta\chi)/\Delta S$. However, although the central line of the shape in Fig. 2 has curvature and torsion, which are due to the abrupt corners not to the in-plane strain. Thus the second and third terms on the right side hand of Eq. (10) should be ignored for SWNTs with out outside forces. Seeing an example, for a helical shape with $K = \frac{R}{R^2+h^2}$ and $\tau = \frac{h}{R^2+h^2}$, we define $\omega = h/R$, there is

$$\Delta\phi = \omega(\Delta\theta - \Delta\chi), \quad (14)$$

here $\Delta\chi$ is the chiral angel difference between two neighbor straight segments. In [12], Zhang *et al.* found $\Delta\phi = \pi/6$, and particularly in Fig. 5a of [12], we can see that two neighbor segments are composed by a zigzag shape and an armchair shape, which indicates $\Delta\chi = -\pi/6$. Moreover, Ou-Yang *et al.*[19] pointed the shape in Fig. 2a of [12] satisfies $\omega = 1$, then substituting the above results into Eq. (14) yields

$$\Delta\theta = 0. \quad (15)$$

This result indicates $\tau + \dot{\chi} \simeq \Delta\theta/\Delta S = 0$ in Eq. (10) strictly. The length for per helix turn is $S_p = 2\pi\sqrt{R^2 + h^2}$, and the segments number for per helix turn is

$$N = \frac{S_p}{\Delta S} = \frac{2\pi}{\Delta\phi} \frac{1}{\sqrt{1 + \omega^2}}. \quad (16)$$

For $\Delta\phi = \pi/6$ and $\omega = 1$, there is $N \simeq 9$. This result is close to the experimental observation that there are about a dozen bends per helix turn [12].

According to the above analysis, to investigate the holistic nature features of SWNTs, the in-plane strain energy should be neglected. Thus the total energy density for SWNTs can be written as

$$\mathcal{F}_t = \frac{\pi k_c}{r_0 \sqrt{1 - r_0^2 K^2}} + \lambda, \quad (17)$$

where λ is the Lagrange multiplier. As to SWNTs, λ can be taken as the average intensity of the effect between a SWNT and its neighbor, such as the dense SWNT ropes model in [35]. For MWNTs, we can take λ as the line tension coefficient due to the effect between one layer of MWNTs and its two neighbor layers. Thus the above energy density in (17) is also suitable to each layers of MWNTs. Comparing Eqs. (11) with (17), we have $\lambda \sim 2\pi r_0 g \sim -10$ eV/nm and $\frac{\lambda r_0}{\pi k_c} \sim -1$. This result will be proved by our later calculations.

One can easily find that the model in (17) will reduce to the string model when $r_0^2 K^2 \ll 1$. Moreover, from (2) to (4), we need $r_0^2 K^2 < 1$ not $r_0^2 K^2 \ll 1$. This small difference will make the model in (17) is suitable for the CNTs shapes with lager deformations and give us much more abundant shapes than the string model. For a 1D elastica structure with the energy density functional $\mathcal{F} = \mathcal{F}(K, \tau)$, the equilibrium shape equations have been obtained in [37, 38] by discussing the first variation of the energy $\delta(\oint \mathcal{F} ds) = 0$. Making use of their results, we attain the equilibrium shape equations for the energy density in (17)

$$\begin{aligned} r_0^2(1 + r_0^2 K^2 - 2r_0^4 K^4) \dot{K} + 3r_0^4 K(3 + 2r_0^2 K^2) \dot{K}^2 \\ - K(1 - r_0^2 K^2)^2(1 - 2r_0^2 K^2 + r_0^2 \tau^2) \\ - \bar{\lambda} K(1 - r_0^2 K^2)^{7/2} = 0, \end{aligned} \quad (18)$$

$$2\dot{K}\tau(1 + 2r_0^2 K^2) + K\dot{\tau}(1 - r_0^2 K^2) = 0, \quad (19)$$

where we define $\bar{\lambda} = \frac{\lambda r_0}{\pi k_c}$. A ring solution with the radius R yields

$$(1 - 2r_0^2/R^2) - \bar{\lambda}(1 - r_0^2/R^2)^{3/2} = 0. \quad (20)$$

According to the experimental results, in most cases there are $0.5 \text{ nm} < r_0 < 5 \text{ nm}$ and $100 \text{ nm} < R < 500 \text{ nm}$ [16, 17], so we have $r_0^2/R^2 \rightarrow 0$, which means $\bar{\lambda} \sim 1$ in Eq. (20). Specially, when $\lambda = 0$ in Eq. (20), we obtain

$$R = \sqrt{2}r_0. \quad (21)$$

This Clifford torus solution for vesicle was found by Ou-Yang [39] and proved by a coming experiment [40]. Avron and Berger [41] gave some details about the torus nearby $R/r_0 = 2$. So the Clifford torus with $R/r_0 = \sqrt{2}$ is easy to be constructed, such as the shapes in series II of Fig. 3 of [42], which are close to this shape.

Substituting the helix solution $K = K_0 \equiv \frac{R}{R^2+h^2}$, $\tau = \tau_0 \equiv \frac{h}{R^2+h^2}$ into Eq. (18) and defining $\omega = h/R$, $\eta = r_0/R$ and the helical angle $\psi_h = \arg \tan \omega$, we have

$$\begin{aligned} (1 + \omega^2)[(1 + \omega^2)^2 + (\omega^2 - 2)\eta^2] \\ + \bar{\lambda}[(1 + \omega^2)^2 - \eta^2]^{3/2} = 0. \end{aligned} \quad (22)$$

We show an example solution in Fig. 3, which is consistent with the values in Fig. 3(b) of [13]. Specially, the zero energy state $\omega = 1$ ($\psi_h = 45^\circ$) [43] yields $\bar{\lambda} = -2/\sqrt{4 - \eta^2}$. If $\lambda = 0$, Eq. (22) is reduced to

$$\eta^2 = \frac{(1 + \omega^2)^2}{2 - \omega^2}. \quad (23)$$

Considering $0 < \eta < 1$, this equation indicates $\frac{\sqrt{2}}{2} \leq \eta < 1$, $\omega^2 < (\sqrt{13} - 3)/2 \simeq 0.3$ and the helix angle $\psi_h < 28.8^\circ$. However, when $\frac{\sqrt{2}}{2} < \eta \leq 0.764$, the shapes are self-intersected. The valid region is $0.764 < \eta < 1$ ($14.1^\circ < \psi_h < 28.8^\circ$) and these shapes are close to the C_{1080} shape in Fig. 1(b) of [44].

Particularly, if $\eta = 1$ and $\omega \rightarrow \infty$ in (22), we obtain a cylinder solution. However, if $\eta = 1$ but ω is finite, what kind of shape we can obtain? If so, we will see that it is nothing but the chiral configuration. Supposing that the state with $\eta = 1$ and $\omega \rightarrow \infty$ is the zigzag shape which has two sp^2 bonds of each carbon hexagon paralleled to the axial line of the SWNT and has the chiral angle $\psi_h = \pi/2$, so the armchair state should be with $\psi_h = \pi/3$ [45] (Note

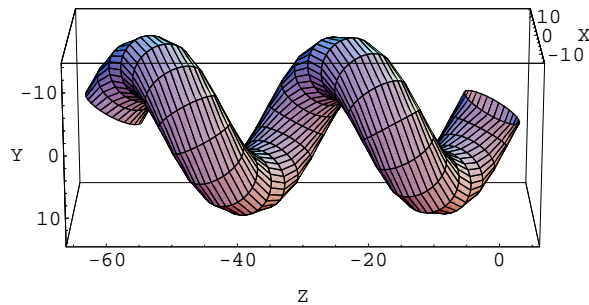


FIG. 3: A helical shape with $R = 9$ nm, $r_0 = 5$ nm, pitch $H_p = 2\pi h = 30$ nm and $\bar{\lambda} = -0.938$ in Eq. (22). This shape is in good agreement with the experimental shape in Fig. 3(b) of [13].

that the chiral angle ψ_h in this paper is the complement angle for the definiens in [45]). Here we define the reduced total energy density for equilibrium helical shapes: $\Omega = \frac{r_0}{\pi k_c} \mathcal{F}_t^0$, using the method in [43], there is

$$\begin{aligned} \Omega &= \frac{r_0}{\pi k_c} [(K_0^2 - \tau_0^2) \mathcal{F}_1^0 + 2K_0\tau_0\mathcal{F}_2^0] / K_0 \\ &= \frac{(1 - \omega^4)\eta^2}{[(1 + \omega^2)^2 - \eta^2]^{3/2}}, \end{aligned} \quad (24)$$

where $\mathcal{F}_1 = \frac{\partial \mathcal{F}_t}{\partial K}$, $\mathcal{F}_2 = \frac{\partial \mathcal{F}_t}{\partial \tau}$, and $\mathcal{F}^0 = \mathcal{F}|_{K=K_0, \tau=\tau_0}$. For straight shapes with $\eta = 1$, equilibrium condition $\partial\Omega/\partial\omega = 0$ yields

$$\omega \rightarrow \infty, \quad \omega = \sqrt{\frac{1}{3}(10^{2/3} + 10^{1/3} + 1)}. \quad (25)$$

These correspond to $\psi_h = \pi/2$ and $\psi_h = 58.2^\circ \approx \pi/3$, respectively. We show $\Omega = \Omega(\psi_h)$ in Fig. 4 which indicates that the chiral angle difference between two equilibrium states is about $\pi/6$. In fact, the 2D continuous model in (17) can not tell us which state in (25) is the zigzag shape. However, it gives us the angle difference between two equilibrium states. This angle difference $\Delta\psi_h = 31.8^\circ \approx \pi/6$ is in good agreement with the lattice model. Further, considering that each carbon hexagon has the area $s_0 = 3\sqrt{3}d^2/2$ and possesses two carbon atoms, where $d = 1.42$ Å is the equilibrium distance of two neighbor carbon atoms, the energy for each carbon atom is

$$E = \frac{\mathcal{F}_t^0}{4\pi r_0} s_0 = \frac{3\sqrt{3}k_c d^2}{8r_0^2} \frac{1 + \omega^2}{\sqrt{(1 + \omega^2)^2 - \eta^2}}, \quad (26)$$

where the unit for r_0 is Å and $\lambda = 0$. Then choosing $k_c = 1.62$ eV, [22] we have $E = \frac{2.1217}{r_0^2}$ and $E = \frac{2.20869}{r_0^2}$ for the two equilibrium states in (25) (note $\eta = 1$), respectively. We simulated the corresponding values in [46] obtained by QMD method and found that the energy for each carbon atoms satisfies $E = \frac{2.05765}{r_0^2}$ for zigzag shapes and $E = \frac{2.08964}{r_0^2}$ for armchair shapes. Clearly, the result obtained by the continuous method in (26) is close to the corresponding result obtained by QMD method, and it also indicates the two states in (25) are the zigzag shape and the armchair shape, respectively. If we want that the result in (26) can consistent with the QMD result in [46] more exactly, we can choose $k_c = 1.55$ eV. Moreover, for a chiral shape with $\eta = 1$ and $\omega \neq 0$, and a helical shape with $\eta < 1$ and the same ω as the chiral shape, Eq. (26) indicates the helical shape will have lower energy for each atom. It explains why there are so many helical shapes are found in experiments. The above results indicate that the continuous model in (17) which based on taking the sp^2 bonds as the geodesic lines on a tube also contains a little information about the lattice structure.

B. Numerical results

Let the central line of the SWNT be $\mathbf{R} = \{R_x, R_y, R_z\}$, $\dot{R}_x = \cos\theta \cos\varphi$, $\dot{R}_y = \cos\theta \sin\varphi$ and $\dot{R}_z = \sin\theta$, where $\theta = \theta(s)$ and $\varphi = \varphi(s)$ are two Euler angles with the variable s , there are

$$K^2 = \dot{\theta}^2 + \dot{\varphi}^2 \cos^2\theta, \quad (27)$$

$$\tau K^2 = \dot{\varphi}(2\dot{\theta}^2 + \dot{\varphi}^2 \cos^2\theta) \sin\theta + (\dot{\varphi}\ddot{\theta} - \dot{\theta}\ddot{\varphi}) \cos\theta. \quad (28)$$

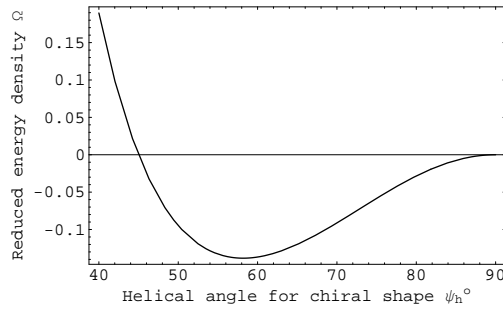


FIG. 4: The chart of the reduced total energy $\Omega = \Omega(\psi_h)$ in (24) with $\eta = 1$ for chiral shapes. It indicates that the chiral angle difference between two equilibrium states is $\Delta\psi_h = 31.8^\circ \approx \pi/6$, which is consistent with the lattice model.

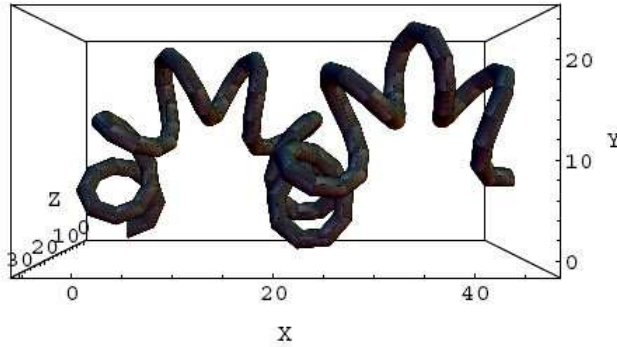


FIG. 5: A positive super helical shape with the initial conditions: $r_0 = 1$ nm, $\bar{\lambda} = -0.978$, $\theta(0) = \varphi(0) = \dot{\varphi}(0) = 0$, $\dot{\theta}(0) = 0.04$ nm⁻¹, $\dot{\varphi}(0) = 0.26$ nm⁻¹ and $\ddot{\theta}(0) = 0.01$ nm⁻². The first helix is right-handed and the second helix is left-handed.

Substituting the above expressions into Eqs. (18) and (19), we obtain two tedious third order equations about θ and φ (see appendix B). Solving this two equations, we obtain several interesting shapes. Fig. 5 shows a positive super helical tube, Fig. 6 shows a negative super helix tube and Fig. 7 shows a right handed helical ring. Experimental basketwork in Fig. 2(b) of [47] which contains many super helical MWNT shapes has excellent mechanical capabilities. As to these unattached super helical shapes in Fig. 5 and Fig. 6, we can conclude that they have strong and restorable retractility like the DNA chain. So, they are perfect functional materials and have large potential in constructing nano-instruments.

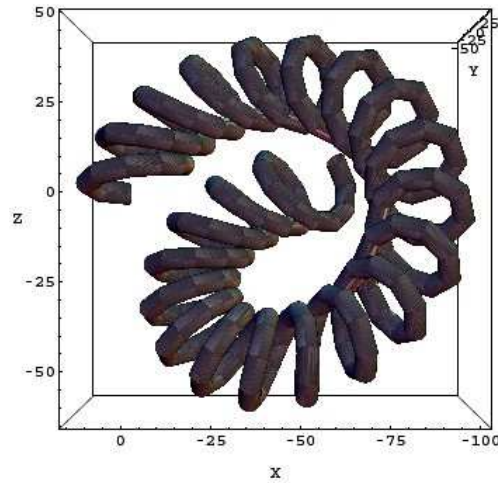


FIG. 6: A negative super helical shape with the initial conditions: $r_0 = 3$ nm, $\bar{\lambda} = -0.97$, $\theta(0) = \varphi(0) = 0$, $\dot{\theta}(0) = 0.018$ nm⁻¹, $\dot{\varphi}(0) = 0.08$ nm⁻¹, $\ddot{\theta}(0) = 0.0009$ nm⁻² and $\ddot{\varphi}(0) = 0.0011$ nm⁻². The first and the second helices are right-handed.

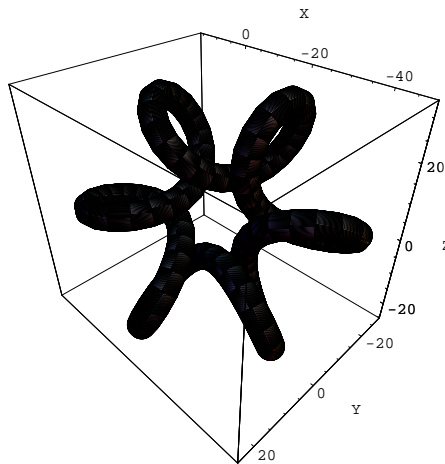


FIG. 7: A right-handed helical ring with the initial conditions: $r_0 = 3$ nm, $\bar{\lambda} = -0.96$, $\theta(0) = \varphi(0) = 0$, $\dot{\theta}(0) = 0.002$ nm $^{-1}$, $\dot{\varphi}(0) = 0.07$ nm $^{-1}$, $\ddot{\theta}(0) = 0.002$ nm $^{-2}$ and $\ddot{\varphi}(0) = 0.00261$ nm $^{-2}$.

In the planar case, the valid shape equation (18) is reduced to

$$r_0^2(1 + \Upsilon^2 - 2\Upsilon^4)\ddot{\Upsilon} + 3r_0^2\Upsilon(3 + 2\Upsilon^2)\dot{\Upsilon}^2 - \Upsilon(1 - \Upsilon^2)^2(1 - 2\Upsilon^2) - \bar{\lambda}\Upsilon(1 - \Upsilon^2)^{7/2} = 0, \quad (29)$$

where $\Upsilon = r_0K$. This is a non-linear equation and it is difficult to be solved generally. We numerically solved this equation but all the solutions we obtained are similar to the shapes in Fig. 4 of [48].

IV. CONCLUSIONS

In conclusion, we have shown a connection between the elastic shell model and the Kirchhoff elastic rod model. Combining Refs. [19, 21] and this work, a complete method to deal with CNTs has been constructed. From lattices model to 2D continues elastic shell model and further to 1D continues elastic rod model, this method gives a recommendable approach to deal with the multi-scale low dimensional systems. The 1D model in (9) which contains the in-plane strain energy is suitable to investigate the mechanical behaviors of CNTs. But we should note that the first term on the right hand side of (9) is the distinct difference, when compared with the isotropic Kirchhoff elastic rod model. This difference will make CNTs have unusual mechanical behaviors which have not been known. Moreover, we should note that the model in (10) is obtained by taken CNTs as isotropic perfect tubes. If there are plenty of pentagonal and heptagonal defects for bended CNTs, this model seems need to be changed. A simple way to adapt this change is to adjust the constants k_c and k_d , such as the work in [34] where the authors chose $k_c = 1.4$ eV which is different to the value $k_c = 1.62$ eV in [22].

For straight chiral CNTs, our study indicates that the difference of the chiral angle between two equilibrium states is about $\pi/6$, which is consistent with the angle difference between the zigzag shape and the armchair shape obtained by lattice model. Our study also reveals that, if a helical shape and a straight chiral shape have the same radius r_0 and the same ω , the former structure will have lower energy for per atom than the later one, which explains why there are so many helical CNTs in experiments. Since there are super helical solutions for the equilibrium shape equations, we hope they can be found in future experiments and the super retractility also can be found for these shapes (If it is only the string model [19], there are only helical solutions but not super helical shapes [49]). How to produce super helical CNTs in experiments? Yin *et al.* [50] provided a way to construct the super CNTs using a cylindrical template. If we choose a helical template, super helical CNTs may be available.

Finally, we would like to point out that how to use the lattice model to construct the super helical CNTs needs further discussion, which will be our future work.

Acknowledgements

The author would like to thank Zhanchun Tu, Weihua Mu and Jianlin Liu for helpful suggestions.

-
- [1] S. Iijima, *Nature (London)* **354**, 56 (1991).
 - [2] W. A. de Heer, A. Chatelain, and D. Ugarte, *Science* **270**, 1179 (1995).
 - [3] H. Dai, J. H. Hafner, A. G. Rinzler, D. T. Colbert, and R. E. Smalley, *Nature (London)* **384**, 147 (1996).
 - [4] S. S. Wong, E. Joselevich, A. T. Wooley, C. L. Cheung, and C. M. Lieber, *Nature (London)* **394**, 52 (1998).
 - [5] S. J. Tans, M. H. Devoret, H. Dai, A. Thess, R. E. Smalley, L. J. Geerligs and C. Dekker, *Nature (London)* **386**, 474 (1997).
 - [6] M. Terrones, N. Grobert, J. Olivares *et al.*, *Nature (London)* **388**, 52 (1997).
 - [7] V. A. Davis, A. N. G. Parra-Vasquez, M. J. Green *et al.*, *Nat. Nanotechnol.* **4**, 830 (2009).
 - [8] L. Wang, Q. Zheng, J. Z. Liu, and Q. Jiang, *Phys. Rev. Lett.* **95**, 105501 (2005).
 - [9] S. Iijima and T. Ichihashi, *Nature (London)* **363**, 603 (1993).
 - [10] A. Thess, R. Lee, P. Nikolaev *et al.*, *Science* **273**, 483 (1996).
 - [11] C. Dekker, *Phys. Today* **52**, 22 (1999).
 - [12] X. B. Zhang, X. F. Zhang, D. Bernaerts, G. Van Tendeloo, S. Amelinckx, J. Van Landuyt, V. Ivanov, J. B. Nagy, Ph. Lambin, and A. A. Lucas, *Europhys. Lett.* **27**, 141 (1994).
 - [13] V. Ivanov, J. B. Nagy, Ph. Lambin, A. Lucas, X. B. Zhang, X. F. Zhang, D. Bemaerts, G. Van Tendeloo, S. Amelinckx, and J. Van Landuyt, *Chem. Phys. Lett.* **223**, 329 (1994).
 - [14] M. Zhang, Y. Nakayama and L. Pan, *Jpn. J. Appl. Phys.* **39**, L 1242 (2000).
 - [15] M. Zhang and J. Li, *Mater. Today* **12**, 12 (2009).
 - [16] R. Martel, H. R. Shea, and P. Avouris, *J. Phys. Chem. B* **103**, 7553 (1999).
 - [17] A. E. Cohen and L. Mahadevan, *Proc. Natl. Acad. Sci.* **100**, 12141 (2003).
 - [18] B. I. Dunlap, *Phys. Rev. B* **50**, 8134 (1994).
 - [19] Z. C. Ou-Yang, Z. B. Su and C. L. Wang, *Phys. Rev. Lett.* **78**, 4055 (1997).
 - [20] M. R. Falvo, G. J. Clary, R. M. Taylor, V. Chi, F. P. Brooks Jr, S. Washburn and R. Superfine, *Nature (London)* **389**, 582 (1997).
 - [21] Z. C. Tu and Z. C. Ou-Yang, *Phys. Rev. B* **65**, 233407 (2002).
 - [22] Z. C. Tu and Z. C. Ou-Yang, *J. Comput. Theor. Nanosci.* **5**, 422 (2008).
 - [23] T. Lenosky, X. Gonze, M. Teter, and V. Elser, *Nature (London)* **355**, 333 (1992).
 - [24] Z. C. Ou-Yang and W. Helfrich, *Phys. Rev. Lett.* **59**, 2486 (1987).
 - [25] D.J. Struik, *Lectures on classical differential geometry* (2nd ed., Constable and Company, Dover, UK, 1988), pp.13-15.
 - [26] L. D. Landau and E. M. Lifshiz, *Theory of Elasticity* (2nd ed., Pergamon, Oxford, 1986).
 - [27] B. I. Yakobson, C. J. Brabec, and J. Bernholc, *Phys. Rev. Lett.* **76**, 2511 (1996).
 - [28] B. I. Yakobson and P. Avouris, *Carbon Nanotubes*, edited by M. S. Dresselhaus and P. Avouris (Springer-Verlag, Berlin, 2001), p287-327.
 - [29] E. Cadelano, S. Giordano and L. Colombo, *Phys. Rev. B* **81**, 144105 (2010).
 - [30] D.A. Kessler and Y. Rabin, *Phys. Rev. Lett.* **90** 024301 (2003).
 - [31] M. P. Do Carmo, *Differential Geometry of Curves and Surfaces*, (1st ed., Prentice-Hall, New York, 1976), p264-283.
 - [32] A. F. da Fonseca and D. S. Galvão, *Phys. Rev. Lett.* **92**, 175502 (2004).
 - [33] L. A. Girifalco and R. A. Lad, *J. Chem. Phys.* **25**, 693 (1956).
 - [34] N. G. Chopra, L. Benedict, V. Crespi, M. Cohen, S. Louie, and A. Zettl, *Nature (London)* **377**, 135 (1995).
 - [35] S. L. Zhang, S. M. Zhao, M. G. Xia, E. H. Zhang, X. J. Zuo, and T. Xu, *Phys. Rev. B* **70**, 035403 (2004).
 - [36] X. F. Zhang and Z. Zhang, *Phys. Rev. B* **52**, 5313 (1995).
 - [37] R. Capovilla, C. Chryssomalakos, and J. Guven, *J. Phys. A: Math. Gen.* **35**, 6571 (2002).
 - [38] N. Thamwattana, J. A. McCoy, and J.M. Hill, *Q. J. Mech. Appl. Math.* **61**, 431 (2008).
 - [39] Z. C. Ou-Yang, *Phys. Rev. A* **41**, 4517 (1990).
 - [40] M. Mutz and D. Bensimon, *Phys. Rev. A* **43**, 4525 (1991).
 - [41] J. E. Avron and J. Berger, *Phys. Rev. A* **51**, 1146 (1995).
 - [42] C. Chuang, Y. C. Fan and B. Y. Jin, *J. Chem. Inf. Model.* **49**, 361 (2009).
 - [43] X. H. Zhou, *Mod. Phys. Lett. B*, **24**, 2403 (2010).
 - [44] S. Ihara, S. Itoh and J.I. Kitakami, *Phys. Rev. B* **48**, 5643 (1993).
 - [45] S. L. Zhang, S. M. Zhao, J. Y. Lü, and M. G. Xia, *Phys. Rev. B* **61**, 12693 (2000).
 - [46] G. B. Adams, O. f. Sankey, J. B. Page, M. O’Keeffe, and D. A. Drabld, *Science* **256**, 1792 (1992).
 - [47] M. Zhang, K. R. Atkinson and R. H. Baughman, *Science* **306**, 1358 (2004).
 - [48] X. H. Zhou, *Chin. Phys. B* **19**, 058702 (2010).
 - [49] J. Langer and D. A. Singer, *J. Differ. Geom.* **20**, 1 (1984); *J. London Math. Soc.* **30**, 512 (1984).
 - [50] Y. J. Yin, Y. L. Chen, J. Yin and K.Z. Huang, *Nanotechnology* **17**, 4941 (2006).

Appendix A

Defining (μ, ν) to be the local coordinates on the tube \mathbf{Y} , where μ is along the tangent of the central line of the tube \mathbf{R} and ν is upright to \mathbf{R} , there are $d\mu = ds$ and $d\nu = r_0 d\theta$. Making use of the Frenet formulae, we obtain

$$E = \mathbf{Y}_\mu \cdot \mathbf{Y}_\mu = (1 - r_0 K \cos \theta)^2 + r_0^2 \tau^2, \quad (\text{A1})$$

$$F = \mathbf{Y}_\mu \cdot \mathbf{Y}_\nu = r_0 \tau, \quad (\text{A2})$$

$$G = \mathbf{Y}_\nu \cdot \mathbf{Y}_\nu = 1, \quad (\text{A3})$$

where $\mathbf{Y}_\mu = \partial \mathbf{Y} / \partial \mu$. The main normal vector of the tube is

$$\mathbf{n} = \frac{\mathbf{Y}_\mu \times \mathbf{Y}_\nu}{|\mathbf{Y}_\mu \times \mathbf{Y}_\nu|} = \mathbf{r} / r_0. \quad (\text{A4})$$

Consequently we obtain

$$L = \mathbf{Y}_{\mu\mu} \cdot \mathbf{n} = K \cos \theta (1 - r_0 K \cos \theta)^2 - r_0 \tau^2, \quad (\text{A5})$$

$$M = \mathbf{Y}_{\mu\nu} \cdot \mathbf{n} = -\tau, \quad (\text{A6})$$

$$N = \mathbf{Y}_{\nu\nu} \cdot \mathbf{n} = -1/r_0. \quad (\text{A7})$$

The mean curvature and Gaussian curvature are

$$H = \frac{LG - 2MF + NE}{2(EG - F^2)} = \frac{1 - 2r_0 K \cos \theta}{2r_0(r_0 K \cos \theta - 1)}, \quad (\text{A8})$$

$$\Lambda = \frac{LN - M^2}{EG - F^2} = \frac{K \cos \theta}{r_0(r_0 K \cos \theta - 1)}. \quad (\text{A9})$$

Appendix B

In this part, we show the shape equations (18) and (19) with the Euler angles as variables. Substituting expressions (27) and (28) into Eqs. (18) and (19), we obtain two tedious equations

$$\begin{aligned} & 4r_0^2 (\dot{\theta} \dot{\varphi}^2 \sin \theta \cos \theta - \dot{\theta} \ddot{\theta} - \dot{\varphi} \ddot{\varphi} \cos^2 \theta)^2 \\ & \times \left\{ 8r_0^2 (\dot{\theta}^2 + \dot{\varphi}^2 \cos^2 \theta) [1 + r_0^2 (\dot{\theta}^2 + \dot{\varphi}^2 \cos^2 \theta)] - 1 \right\} \\ & + 4r_0^2 \left\{ 1 + r_0^2 (\dot{\theta}^2 + \dot{\varphi}^2 \cos^2 \theta) [1 - 2r_0^2 (\dot{\theta}^2 + \dot{\varphi}^2 \cos^2 \theta)] \right\} \\ & \times (\dot{\theta}^2 + \dot{\varphi}^2 \cos^2 \theta) (\ddot{\theta}^2 + \ddot{\varphi}^2 \cos^2 \theta - \dot{\theta}^2 \dot{\varphi}^2 \cos 2\theta \\ & - \ddot{\theta} \dot{\varphi}^2 \sin \theta \cos \theta - 2\dot{\theta} \dot{\varphi} \ddot{\varphi} \sin 2\theta + \dot{\theta} \dot{\theta}^{(3)} + \dot{\varphi} \dot{\varphi}^{(3)} \cos^2 \theta) \\ & - 4 [1 - r_0^2 (\dot{\theta}^2 + \dot{\varphi}^2 \cos^2 \theta)]^2 \times \left\{ (\dot{\theta}^2 + \dot{\varphi}^2 \cos^2 \theta)^2 \right. \\ & \times \left[1 - 2r_0^2 (\dot{\theta}^2 + \dot{\varphi}^2 \cos^2 \theta) + \bar{\lambda} (1 - r_0^2 (\dot{\theta}^2 + \dot{\varphi}^2 \cos^2 \theta))^{3/2} \right] \\ & \left. + r_0^2 [2\dot{\theta}^2 \dot{\varphi} \sin \theta + \dot{\varphi} \cos \theta (\dot{\varphi}^2 \sin \theta \cos \theta + \ddot{\theta}) - \dot{\theta} \dot{\varphi} \cos \theta]^2 \right\} \\ & = 0, \end{aligned} \quad (\text{B1})$$

$$\begin{aligned}
& (\ddot{\theta}\dot{\theta} + \dot{\varphi}\ddot{\varphi}\cos^2\theta - \dot{\theta}\dot{\varphi}^2\sin\theta\cos\theta) [1 + 2r_0^2(\dot{\theta}^2 + \dot{\varphi}^2\cos^2\theta)] \\
& \times 2 [2\dot{\theta}^2\dot{\varphi}\sin\theta + \dot{\varphi}\cos\theta(\dot{\varphi}^2\sin\theta\cos\theta + \ddot{\theta}) - \dot{\theta}\ddot{\varphi}\cos\theta] \\
& + [1 - r_0^2(\dot{\theta}^2 + \dot{\varphi}^2\cos^2\theta)] \left\{ 2\dot{\theta}^5\dot{\varphi}\cos\theta + 3\dot{\theta}^4\ddot{\varphi}\sin\theta \right. \\
& \quad + \dot{\varphi}^2\cos^3\theta(\dot{\varphi}^2\ddot{\varphi}\sin\theta\cos\theta - 2\ddot{\theta}\dot{\varphi} + \dot{\varphi}\theta^{(3)}) \\
& \quad + \dot{\theta}^2\cos\theta(2\ddot{\theta}\dot{\varphi} + \dot{\varphi}\theta^{(3)}) + \frac{1}{4}\dot{\theta}^3[\dot{\varphi}^3(11\cos\theta + \cos 3\theta) \\
& \quad - 4\ddot{\theta}\dot{\varphi}\sin\theta - 4\varphi^{(3)}\cos\theta] + \dot{\varphi}\dot{\theta}\cos\theta[3\dot{\varphi}^2\ddot{\theta}\sin\theta\cos\theta - 2\ddot{\theta}^2 \\
& \quad \left. + \cos^2\theta(\dot{\varphi}^4\cos^2\theta + 2\ddot{\varphi}^2 - \dot{\varphi}\varphi^{(3)}) \right\} \\
& = 0.
\end{aligned} \tag{B2}$$

Solving the above equations, we get $\theta = \theta(s)$ and $\varphi = \varphi(s)$, and consequently obtain $R_x = \int_0^S \cos\theta \cos\varphi ds$, $R_y = \int_0^S \cos\theta \sin\varphi ds$ and $R_z = \int_0^S \sin\theta ds$. The SWNT shape can be written as

$$\begin{aligned}
\mathbf{Y} &= \{X, Y, Z\}, \\
X &= (\dot{\theta}^2 + \dot{\varphi}^2\cos^2\theta)^{-\frac{1}{2}} [r_0 \sin\varphi(\dot{\theta}\sin\phi - \dot{\varphi}\cos\theta\cos\phi) \\
& \quad - r_0 \sin\theta \cos\varphi(\dot{\theta}\cos\phi + \dot{\varphi}\cos\theta\sin\phi)] + R_x,
\end{aligned} \tag{B3}$$

$$\begin{aligned}
Y &= (\dot{\theta}^2 + \dot{\varphi}^2\cos^2\theta)^{-\frac{1}{2}} [r_0 \cos\varphi(\dot{\varphi}\cos\theta\cos\phi - \dot{\theta}\sin\phi) \\
& \quad - r_0 \sin\theta \sin\varphi(\dot{\theta}\cos\phi + \dot{\varphi}\cos\theta\sin\phi)] + R_y,
\end{aligned} \tag{B4}$$

$$\begin{aligned}
Z &= r_0 \cos\theta (\dot{\theta}^2 + \dot{\varphi}^2\cos^2\theta)^{-\frac{1}{2}} (\dot{\theta}\cos\phi + \dot{\varphi}\cos\theta\sin\phi) \\
& \quad + R_z.
\end{aligned} \tag{B5}$$